RSC Advances

ROYAL SOCIETY OF CHEMISTRY

www.rsc.org/advances

Journal Name

ARTICLE

AlN-based Film Buck Acoustic Resonator Operated in Shear Mode for Detection of Carcinoembryonic Antigens

Received 00th January 20xx,
Accepted 00th January 20xx

DOI: 10.1039/x0xx00000x

www.rsc.org/

Dan Zheng [a, b], Juan Xiong [a, *], Peng Guo [a], Shengfu Wang [c], Haoshuang Gu[a, *]

A film buck acoustic resonator (FBAR) operated in shear mode was fabricated and integrated with a microchannel for detection of the carcinoembryonic antigens (CEA). C-axis inclined aluminium nitride (AlN) film was deposited on the Bragg reflector by rotating the substrate holder plate using a reactive magnetron sputtering. The polydimethylsiloxane (PDMS) microchannel was integrated with the fabricated resonator. The XRD results exhibited coexisting (002) and (101) orientations corresponding to the c-axis inclined AlN film. The resonant frequency of the FBAR was located near at 1.2 GHz. The average electromechanical coupling factor K_{eff}^2 and quality factor Q were 3.19% and 170, respectively. The frequency shift of the biosensor was proportionately increased as the concentration of the immobilized anti-CEA aptamer increased. The CEA binding ratio was initially increased with antibody concentration reaching a highest value at 47.04%. The mass sensitivity of the fabricated biosensor was calculated to be approximately 2045.89 Hz cm²/ng.

1. Introduction

Biosensors have become very popular in the research community for their potential biotechnological and biomedical applications such as medical analysis and diagnosis.[1-6] The film buck acoustic resonator offers several analytical advantages such as simplicity of operation, high sensitivity, small size, low power consumption and low cost.[7-13] However, FBAR is usually operated in a purely longitudinal thickness mode, which can cause severe dissipation of the acoustic energy into the sample liquid resulting in the poor quality factor and a decrease of mass sensitivity.[14] On the other hand, in the FBAR the particle displacement of the shear mode acoustic wave is parallel to the film surface. Consequently, compression is not produced in the liquid, so there is little energy leakage damping in the liquid. Therefore, in liquid, the shear mode wave is more suitable than the longitudinal mode wave.[14-18] For a given FBAR configuration, the c-axis inclined piezoelectric film is feasible for excitation of the shear mode wave, and the shear mode will result with inclinations of greater than 10° already. [19]

When FBAR sensors are used as a biosensor, a common detection method is to drop the analyte on the active area of the FBAR, which affects the final test results. For accurate measurements, attempts have been made to fabricate microchannels on the active area and place the targeted analyte onto the biosensor surface under low disturbance and stable flow conditions. PDMS provides an alternative analyte sampling approach and demonstrates its remarkable advantages, including easy operation, low reagent consumption, lower time-consumption and easy transplantation.[14, 20] The integrated FBAR and PDMS microfluidic provides a compact system for the measurements in liquid environments.

This reported study describes an integrated FBAR-PDMS biosensor operated in shear mode, which contained an immobilized anti-CEA aptamer for detection of CEA. Anti-CEA aptamers are select functional DNA or RNA sequences that can be immobilized on an Au electrode via Au-S sulfhydryl bond, which can strongly adsorb corresponding targeted CEA due to their specific binding affinity.[21, 22] The characteristics of the fabricated FBAR-PDMS sensor were monitored and evaluated in a gas-liquid environment. After FBAR-PDMS sensor was modified with an anti-CEA aptamer sensitive bio-layer, the performance of the device was investigated. In addition, the dependence of the mass loading on various anti-CEA aptamer concentrations and CEA binding ratio was examined and discussed.

2. Experimental

2.1. Reagents

CEA (95%, SDS-PAGE) was purchased from Sigma-Aldrich (USA) and the anti-CEA binding aptamer sequences (30-SH-ATACCAGCTTATTCAATT-50) were purchased from Sangon (Shanghai, China). Tris-HCl buffer (50 mM Tris–HCl, 300 mM NaCl, pH 8.0) and other reagents were analytical grade. An SU-8

[a] Hubei Collaborative Innovation Center for Advanced Organic Chemical Materials, Faculty of Physics & Electronic Science, Hubei University, Wuhan 430062, China.
[b] Faculty of Electronic and Engineering, Vocational College of WuHan Software Engineering, WuHan 430205, China.
[c] Faculty of Chemistry and Chemical Engineering, Hubei University, Wuhan 430062, China.
* Corresponding author Email: guhsh@hubu.edu.cn.

negative photoresist was purchased from the Microlithography Chemical Corp (Newton, MA, USA). A firming agent and PDMS were purchased from Dow Corning Corporation (Midland MI, USA).

2.2. Configuration of the integrated FBAR and PDMS microfluidic system

The basic configuration of the FBAR and the PDMS microfluidic system is shown in **Fig. 1(a)**. To prevent dissipation of the acoustic energy into the substrate, three alternative pairs of Ti/Mo were deposited on Si substrate using DC magnetron sputtering, which constituted a high and low impedance Bragg stack reflector. Each layer of the Bragg reflector had a λ/4 thickness to achieve the acoustic mirror response. The AlN thin films were reactively RF deposited on the Bragg stack with a magnetron sputtering system (JGP 450) and the Al metal target was a 60 mm in diameter with 99.995% purity. The c-axis inclined AlN films were prepared by rotating the substrate holder plate to an optimized angle of 10°. To improve the crystal quality and reduce the roughness between layers, all deposition parameters were optimized.

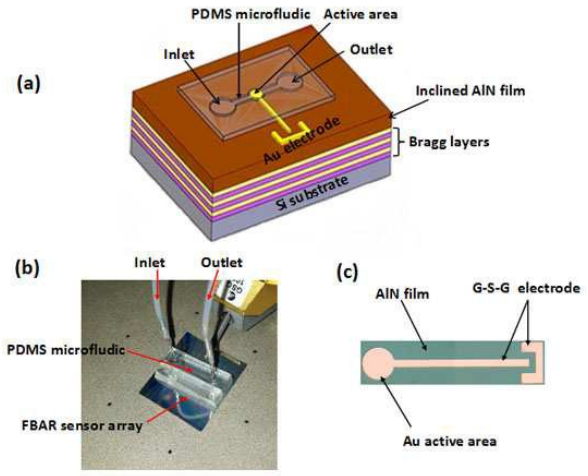

Fig. 1. The integrated FBAR-PMDS sensor: (a) schematic illustration of FBAR integrated with the PDMS microchannel, (b) the photograph of the real device and (c) the picture of single sensor with patterned Au electrode.

A photograph of the actual device is shown in **Fig. 1(b).** The PDMS microfluidic channel was molded onto the FBAR sensor using standard, soft photolithography technology. The SU-8 negative photoresist was spin-coated onto a quartz glass substrate to pattern the microchannel. The main line of microchannel had a width of 300 μm and a height of 100 μm. After the SU-8 mold was fabricated, a mixture of PDMS and a matched firming agent was poured into the mold and cured to make a replicate of the photoetched reverse pattern. Next, the PDMS was peeled from the substrate resulting in a soft rubber patterned microchannel. Then, the outlet and inlet of the device were fabricated using a cylindrical syringe needle to punch the access holes. Finally, the bonding process of PDMS mold and Si substrate was conducted under irradiation of a UV lamp for 3h. The PDMS microchannels were lined up neatly on the active area, as shown in **Fig. 1(a)**.

And **Fig. 1(c)** is potho of the patterned Au electrode, with an active area of 200×200μm^2 on which select biomolecules were immobilized. The connecting line between the ground-single-ground (G-S-G) pad and active area was extended for the microflow passway. As is seen from **Fig. 1**, the FBAR-PDMS based device was fabricated and adapted for measurements in a liquid environment.

2.3. Self-assembly anti-CEA aptamer for detection of CEA

A schematic diagram of the AlN-based FBAR modified with the anti-CEA aptamers sensitive layer for detection of CEA is shown in **Fig. 2**. Description of the detailed process for self-assembly of the antibody sensitive bio-layer is given in our previous work.[23] A fluidic condition simulating the physiological environment was established by injecting fluid using a pump impeller at a constant flow rate (9 μl /min). Before modification, the Au electrode surface should been successively pretreated with acetone, alcohol and deionized water. After complete washing, the microfluidic channel was dried with nitrogen and washed with Tris-HCl buffer to establish a baseline. The bare FBAR-PDMS based device can function in air and fluidic conditions as depicted in **Fig. 2(a)**.

The flow ratio remained unchanged to insure that reproducible results can be obtained in a static system. The anti-CEA aptamer was coated on the active area by an Au-S bond to establish a biorecognition sensitive layer.[22] The microfluidic channel was washed with deionized water and Tris-HCl buffer to remove the unbound anti-CEA aptamers, thereby achieving a well-aligned sensitive bio-layer as shown in **Fig. 2(b)**. The frequency shifts of the modified device were measured in the presence of various antibody concentrations.

As shown in **Fig. 2(c)**, a concentration of CEA solution was injected into the microchannel system to form biochemical interaction, which was reacted for 2 h at the interface at 37 ℃.

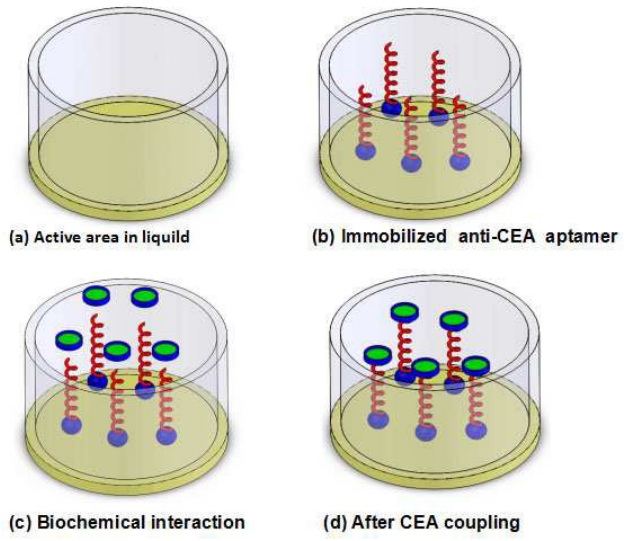

Fig. 2. The schematic illustration of FBAR modified with anti-CEA aptamers to detect CEA: (a) bare FBAR device immersed in liquid, (b) immobilized anti-CEA aptamer, (c) introduced analyte CEA and

Close coupling between the CEA antigen-antibody resulted as shown in **Fig. 2(d)**, and this was followed by rinsing with the Tris–HCl buffer to remove the uncombined CEA. The binding ratio between the CEA and various anti-CEA aptamer concentrations was evaluated. Before measurement of the various liquids, the microfluidic channel was washed using a standard process.

2.4. Testing equipment

The crystal orientation of the FBAR was determined by using X-ray diffraction (XRD, Bruker Advanced D8). The morphologies of the films were examined using field-emission scanning electron microscopy (SEM, JEOL 7100F).

The vector network analyzer (Agilent E5071C, USA) and RF probe station (PE-4, EverBeing, Taiwan) were used as the testing platform, which assisted in analyzing the performance of the integrated FBAR-PDMS device characterized in air and in Tris–HCl buffer with different concentrations of anti-CEA aptamer solution and CEA.

3. Results and discussion

As shown in **Fig. 3(a)** the FBAR consisted of a piezoelectric sandwich (AlN film, Ti/Mo Bragg reflector layers and Si substrate), which constituted the basic composition of the device as depicted in the cross-section SEM image. The magnified AlN film is shown in **Fig. 3(b)**. Inclined AlN columns are clearly visible and can be estimated to be 20° from the surface normal, which ensured excitation of shear mode wave. In **Fig. 3 (c)**, the (002) diffraction peak of the AlN film is evident at 35.9°, which exhibited the preferred c-axis orientation. Simultaneously, the (101) orientation is co-existant corresponding with the c-axis tilted AlN, which enables the sensor excitation of the shear mode wave and is appropriate for

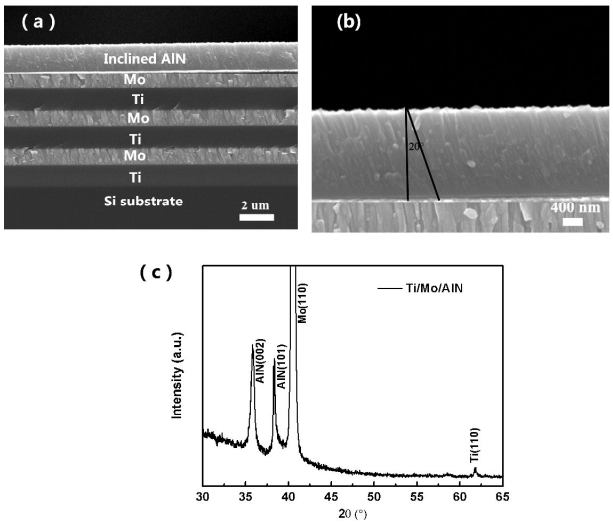

Fig. 3. FBAR based c-axis tilted AlN film: (a) the cross-section scanning electron microscopy image, (b) the amplification of the inclined AlN film, and (c) the XRD pattern.

the applications in liquid conditions. [14-18]

The measured return loss (S_{11}) parameters of the fabricated FBAR-PDMS sensor in air and Tris-HCl buffer are shown in **Fig. 4**, where both the longitudinal and shear modes are obviously observed. The resonance frequency f exhibited a relationship with the piezoelectric film thickness d as $f = v/2d$, and v is the acoustic velocity.[24] The acoustic wave has the shear mode wave and the longitudinal mode, and the acoustic velocity of the latter is larger than the former.[24-26] Consequently, the resonance frequency of the shear mode is smaller than the resonance frequency of longitudinal mode. The resonance frequencies of the shear mode in air and Tris-HCl buffer are located at 1234.7 MHz and 1227.4 MHz, respectively, which can be seen in **Fig. 4.**

Using the formula $f = v/2d$, the calculated average acoustic velocity is 4875 m/s, which is close to 6333 m/s, the theoretical acoustic velocity of shear mode in the AlN film. In addition, the calculated value of 4875 m/s is much lower than the longitudinal acoustic velocity 10,172 m/s of AlN film.[24-26] Therefore, it is believed that the shear mode wave was excited instead of the longitudinal wave.

Fig. 4 also compares the electrical response of both modes in air and liquid media. As can be seen from **Fig. 4**, the return loss S_{11} of the shear mode in the liquid declined slightly, while the S_{11} of the

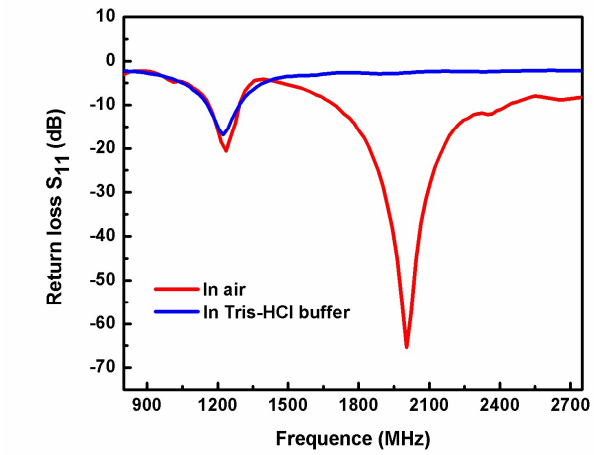

Fig. 4. Returning loss S_{11} curve indicating the performance of the device in air and in Tris-HCl buffer.

longitudinal mode deteriorated and decreased sharply.

In **Fig. 5**, the impedance magnitude and resonant frequency were monitored for the FBAR-PDMS sensor operated in air and in Tris-HCl buffer. The resonant frequency of the shear mode can be clearly seen at around 1.2 GHz in both media, while the longitudinal mode wave was almost completely damped in the liquid, as indicated by the S_{11} curve shown in **Fig. 4.**

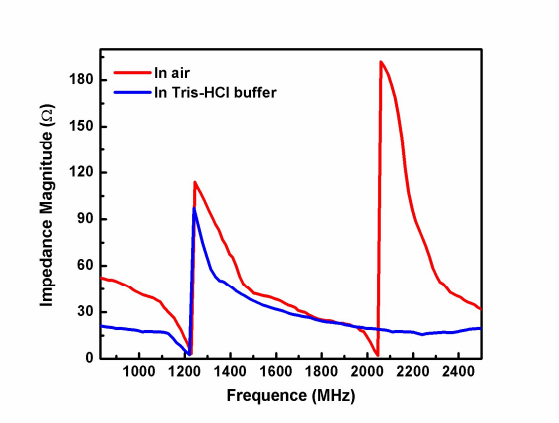

Fig. 5. Impedance characteristics of the device operated in air and Tris–HCl buffer.

This result occurred due to the compression of the longitudinal mode acoustic wave in the liquid, which resulted in the attenuation of the energy as it propagated through the liquid[14, 15] While the shear mode acoustic wave propagates parallel to the film's surface, confining the energy in the liquid. Thus the energy is reflected back from the interface which ensures high performance of the resonator in liquid.[16-18]

The electromechanical coupling coefficient (K_{eff}^2), the quality factor (Q) and the mass sensitivity (S_m) can be calculated using the following equations: [15, 16]

$$K_{eff}^2(\%) = \frac{\pi^2 (f_p - f_s)}{4 f_p} \times 100\% \qquad (1)$$

$$Q = \frac{f_m}{\delta f_{-3dB}} \qquad (2)$$

$$S_m = \frac{\Delta f}{\Delta m} = \frac{2 f_0^2}{A\sqrt{\mu\rho}} \qquad (3)$$

In equation (1), f_s and f_p are the series and parallel resonant frequencies. In equation (2), f_m is the frequency of the peak value and the denominator is the peak breadth at -3 dB. In equation (3), A is the active area, ρ is the density of material, μ is the material stiffness, and Δm is the loading mass at the surface.

Table 1 The performance of the FBAR-PDMS sensor based on 20° c-axis inclined AlN film.

Performance index	In air	In buffer
f_s (GHz)	1.227	1.219
f_p (GHz)	1.246	1.235
Q	193	174
K^2_{eff} (%)	3.75	3.19

Using the these equations and the data shown in **Fig. 5,** the performance of the integrated FBAR-PDMS sensor can be evaluated, which is summarized in **Table 1.** Using equation (1) and (2), the quality factor Q of the shear mode wave was calculated to be 193 in air and 174 in liquid. The corresponding electromechanical coupling factor K_{eff}^2 are 3.75% in air and 3.19% in aqueous Tris–HCl buffer, which indicates that the proposed sensor achieves the expected performance.[26-28]

The anti-CEA aptamer self-assembly was employed on the fabricated devices to detect the CEA antigen. The biosensor self-assembled with various concentrations anti-CEA aptamer was detected. The frequency shift (Δf) of the biosensor modified with various concentrations anti-CEA aptamer ranging from 0.2 to 10 μm/l is shown in **Fig. 6**. The fundamental frequency of the bare FBAR was found to be at 1227.16 MHz with an insertion loss of about −17.07 dB. After modification with 0.2 μm/l anti-CEA aptamer, a frequency shift of 292.02 KHz was observed. According to FBAR sensing theory, a small mass loading change can lead to a resonant frequency shift. [29] After the active area was modified with the bound anti-CEA aptamer, the mass loading of the FBAR increased and the resonance frequency correspondingly decreased. Therefore, it is believed that the anti-CEA aptamer sensitive layer was self-assembled onto the device. Using equation (3), the mass sensitivity S_m of the fabricated biosensor was determined and calculated to be 2045.89 Hz cm^2/ng. In the report by W.C. Xu et al, the mass sensitivity S_m of the shear mode was calculated to be 638 Hz cm^2/ng.[9] The R. Gabl group found that the sensitivity of their FBAR sensor was approximately 2400 Hz cm^2/ng.[13] Finally, the work of J. Weber at el, found that the sensitivity of their FBAR in shear mode was approximately 800 Hz cm^2/ng.[28] In this presently reported study, the resonator functioned best at near 1.2 GHz with Q factors of 193 in air and 174 in liquid. The mass sensitivity value

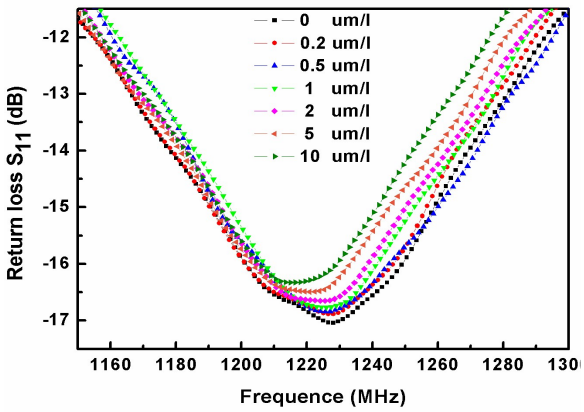

Fig. 6. The frequency shift of FBAR-PDMS biosensor self-assembled with various concentrations anti-CEA aptamer ranging from 0 to 10 um/l.

Table 2 The frequency shift (Δf) of various anti-CEA aptamer concentration and CEA binding ratio.

Concentration of anti-CEA aptamer (um/*l*)	CEA aptamer immobilization Δf (*KHz*)	CEA binding Δf (KHz)	CEA binding ratio
0.2	292.02±22.5	50.22±18.33	17.20%
0.5	876.06±18.6	190.58±22.64	21.75%
1	2044.13±32.5	560.32±33.66	27.41%
2	4380.27±48.5	2060.65±54.31	47.04%
5	8144.06±52.6	2240.65±54.31	27.51%
10	8356.26±55.2	1590.20±52.18	19.03%

Note: **CEA concentration was fixed at 1 um/l.**

was around 2045.89 Hz cm^2/ng, demonstrating the good performance of the biosensor in a liquid medium.[9, 13, 28]

To compare the influence of various concentrations the anti-CEA aptamer on the integrated FBAR-PDMS biosensor, a fixed 1 μm/l CEA solution was injected into the microfluidic system and tested. More than 20 samples were tested. As shown in **Table 2**, the CEA binding ratio[30] initially increased as the concentration of the anti-CEA aptamer increased and reached the highest value of 47.04% when the antibody concentration was 2 μm/l. When the antibody concentration was further increased, the CEA binding ratio decreased.

Fig. 7 shows the curve representing the amount of anti-CEA aptamer immobilization on the biosensor and the subsequent CEA binding ratio. The relationship between the resonant frequency shift Δf and the increase of the antibody concentration under 5 μm/l was nearly linear which complied with the Sauerbrey equation.[29] This was a clear indication of antibody self-assembly on the sensor. When the antibody concentration was greater than 5 μm/l, the relationship between the resonant frequency shift Δf and antibody concentration levelled off, indicating full occupation of the active area by antibody molecules.

With the increasing concentration of anti-CEA aptamer, the CEA binding ratio increased and reached a maximum, then it declined and levelled off, as can be seen in **Fig. 7**. The maximum value occurred at an antibody concentration of around 2 um/l. Above this value, the binding ratio showed a drastic decline with increasing amounts of the antibody, indicating there was a balance between the increase of binding sites and the reduction of reachability.

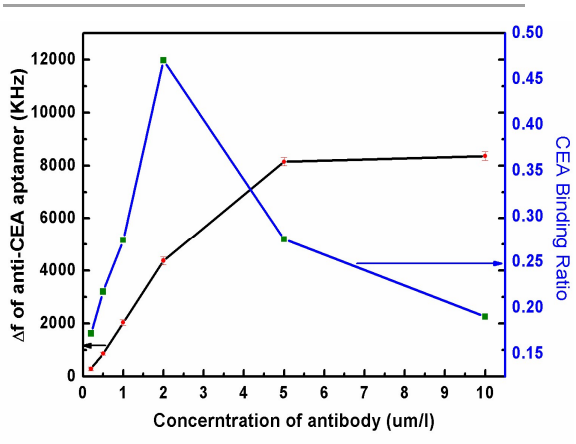

Fig. 7. Frequency shift and CEA binding ratio under various anti-CEA aptamer concentration.

With the increase of antibody concentration, the amount of antigen bond to the immobilized antibody increased due to the increasing of binding sites in the active area. When the antibody concentration was greater than 2 um/l, the active area was fully covered by the antibody and multilayer adsorption began to occur. Many of the binding sites were buried beneath the layer and became unavailable for antigen binding. The binding efficiency became very low and the binding ratio tended to decline with the increasing of antibody concentration, according with the general aspects observed from other antibody-antigen binding systems.[1, 29, 31] Therefore, the optimum concentration of the anti-CEA aptamer was found to be 2 um/l, which is recommended for a FBAR sensor for testing with1 um/l of CEA antigen.

Generally, the serum CEA content in a healthy people is below 5ng/ml.[32] At present, the monitoring level of the device is below the requirement of practical applications. Thus, how to improve the detection limit and test in serum is the following work.

4. Conclusions

An integrated FBAR-PDMS biosensor based on a c-axis inclined AlN film was fabricated and operated in the shear mode for detecting CEA. Reactive magnetron sputtering was used to prepare c-axis inclined AlN film with a mean tilt of around 20° . The XRD results revealed coexistence of (002) and (101) orientations, which corresponded to a c-axis inclined AlN film. The resonant frequency of the FBAR was located near at 1.2 GHz in liquid. The average electromechanical coupling factor K_{eff}^2 and Q factor of the resonators were 3.19% and 170, respectively. To investigate the optimal concentration of antibody required for detecting CEA, an anti-CEA apatamer concentration ranging from 0.2 to 10 um/l was investigated. The resonant frequency shift of the experimental device was increased proportionately with the increase of anti-CEA aptamer concentration in the range of 0.2 to 5um/l. The CEA binding ratio initially increased with anti-CEA aptamer concentration and attained the greatest value of 47.04%.The mass sensitivity of the fabricated sensor was found to be approximately 2045.89 Hz cm^2/ng. The integrated FBAR-PDMS device shows great application potential as a mass loading biosensor in liquid media.

Acknowledgements

The author would like to acknowledge financial support from the National Natural Science Foundation of China (Grant Nos. 11474088, 61106070), the National High Technology Research and Development Program of China (Grant No. 2013AA031903), the Key Project of Natural Science Foundation of Hubei Province of China (Grant No. 2013CFA043, 2014CFB557), and the Natural Science Foundation of Hubei Provincial Department of Education (Grant No. Q20141005).

References

1 X. B. Zhao, F. Pan, G. M. Ashley, L. Garcia-Gancedod, J. Luo, A. J. Flewitt, W. I. Milned, and J. R. Lu, *Sensors and Actuators B*, 2014, **290**, 946-953.
2 I. Voiculescua, A. N. Nordin, *Biosensors and Bioelectronics*, 2012, **33**, 1-9.
3 K. W. Zhang, L. Zhang, Y. S. Chai, *Sensors*, 2015, **15**, 20267-20278.
4 J. C. Andle, and J. F. Vetelino, *Sensors and Actuators,* 1994, **44**, 167-176.
5 K.W. Zhang, L. Zhang, L. L. Fu, S. Q. Li, H. Q. Chen, and Z. Y. Cheng, *Sensors and Actuators*, 2013, **200**, 2-10.
6 X. B Zhao, G. M. Ashley, L. Garcia-Gancedo, H. Jin, J. K. Luo, A. J. Flewitt, J. R. Lu, *Sensors and Actuators*, 2012, **163**, 242-246.
7 A. J. Flewitt, J. K. Luo, Y. Q. Fu, L. Garcia-Gancedo, X. Y. Du, J. R. Lu, X. B. Zhao, E. Iborra, M. Ramose, and W. I. Milne, *Journal of Non-Newtonian Fluid Mechanics*, 2015, **222**, 209–216.
8 G. Wingqvist, Surface & Coating Technology, 2010, **205**, 1279-1286.
9 W. C. Xu, X. Zhang, S. Choi, and J. Chae, *Journal of Microelectromechanical System*, 2011, **20**, 213-220.
10 I. Katardjiev, V. Yantchev, *Vacuum*, 2012, **86**, 520-531.
11 I. Voiculescu, A.N. Nordin, *Biosensors and Bioelectronics*, 2012, **33**, 1-9.
12 M. Nirschl, A. Rantala, K. Tukkiniemi, S. Auer, A. C. Hellgren, D. Pitzer, M. Schreiter, and I.V. Lundin, *Sensors*, 2010, **10**, 4180-4193.
13 R. Gabl, H. D. Feucht, H. Zeininger, G. Eckstein, M. Schreiter, R. Primig, D. Pitzer, and W. Wersing, *Biosensors and Bioelectronics*, 2004, **19** , 615-620.
14 J. Xiong, P. Guo, X. L. Sun, S. F. Wang, M. Z. Hu, and H. S. Gu, *Chinese Physics Letters*, 2014, **31**, 028502 (1-5).
15 C. D. Corso, A. Dickherber, W. D. Hunt, *Journal of Applied Physics*, 2007, **101**, 054514(1-7).
16 M. Penza, P. Aversa, G. Cassano, D. Suriano, W. Wlodarski, M. Benetti, D. Cannatà, F.D. Pietrantonio, and E. Verona, *IEEE Transactions on electron devices*, 2008, **55**, 1237-1243.
17 G. Wingqvist, J. Bjurstr¨ om, L. Liljeholm, V. Yantchev, I. Katardjiev, *Sensors and Actuators B*, 2007, **123** , 466-473.
18 M. Linka, J. Weber, M. Schreiter, W. Wersing, O. Elmazria, and P. Alnot, *Sensors and Actuators B*, 2007, **121**, 372-378.
19 K. Tukkiniemi, A. Rantala, M. Nirschl, D. Pitzer, T. Huber, M. Schreiter, *Procedia Chemistry*, 2009, **1**, 1051-1054.
20 R. C. Stevenson, C. R. Lowe, *Biosensors and Bioelectronics*, 2012, **35**, 425-428.
21 A. D. Ellington, J. W. Szostak, *Nature*, 1990, **346**, 818-822.
22 Y. Lu, X. C. Li, L. M. Zhang, P. Yu, L. Su, and L. Q. Mao, *Analytical Chemistry*, 2008, **80**, 1883-1990.
23 D. Zheng, J. Xiong, P. Guo, Y. B. Li, S. H. Wang, and H. S. Gu, *Materials Research Bulletin*, 2014, **59,** 411-415.
24 D. Chen, J. J. Wang, D. H. Li, Y. Xu, and Z. X. Li, *Sensors and Actuators A*, 2011, **165**, 379-384.
25 D. Chen, J. J. Wang, Y. Xu, D. H. Li, Z. X. Li, and H. W. Song, *Applied Surface Science*, 2010, **256**, 7638-7642.
26 D. Chen, J. J Wang, Y. Xu, and D. H. Li, *Sensors and Actuators B*, 2012, **171-172**, 1081-1086.
27 J. J. Wang, D. Chen, Y. Xu, and W.H. Liu, *Sensors and Actuators B*, 2014, **190**, 378-383.
28 J. Weber, W. M. Albers, J. Tuppurainen, M. Link, R. Gabl, W. Wersing, and M. Schreiter, *Sensors and Actuators A*, 2006, **128**, 84-88.
29 L. García-Gancedoa, J. Pedrós, E. Iborra, M. Clement, X. B. Zhao, J. Olivaresd, J. Capilla, J.K. Luo, J.R. Lu, W.I. Milnea, and A. J. Flewitt, *Sensors and Actuators B*, 2013, **183**, 136-143.
30 T. Y. Lee, J. T. Song, *Thin Solid Films*, 2010, **518**, 6630-6633.
31 H. Xu, J.R. Lu, and D.E. Williams, *Journal of Physical Chemistry B*, 2006, **110**, 1907-1914.
32 D. Moro, D. Villemainb, J.P. Vuillezb, C.A. Delord, C. Brambilla, *Lung Cancer,* 1995, **13**, 169-176.

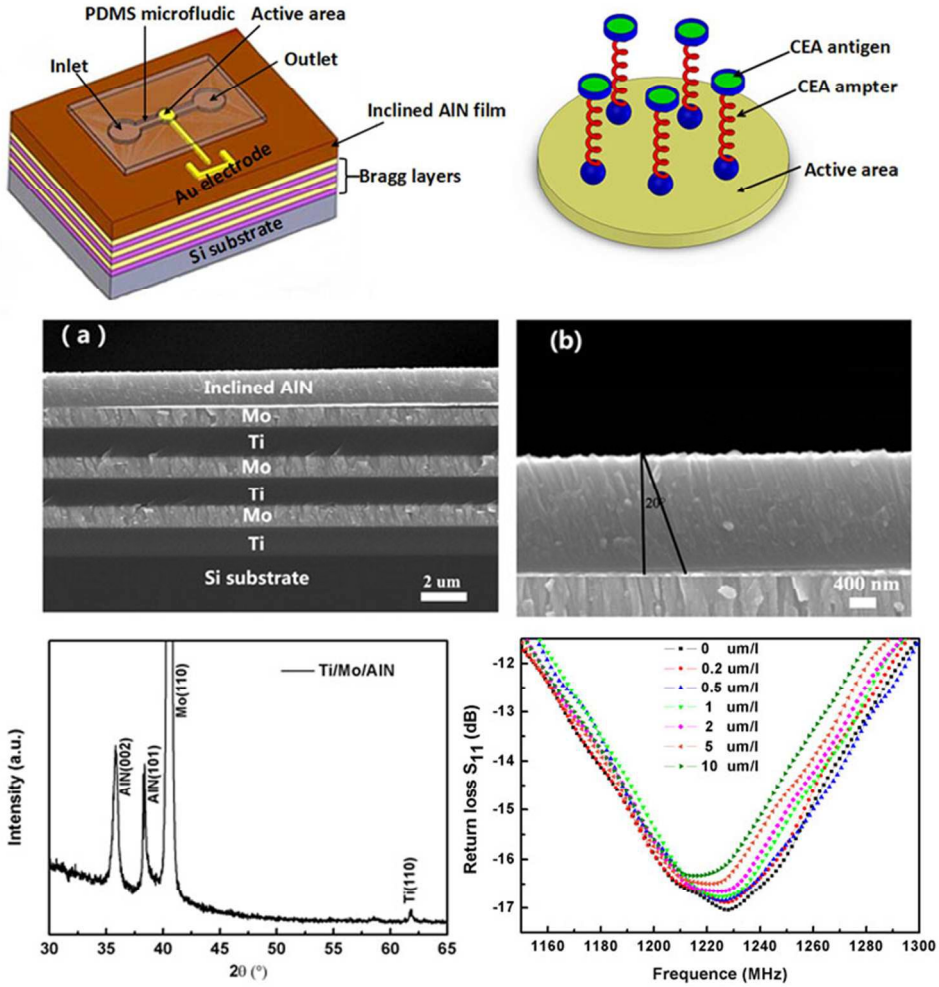

299x299mm (72 x 72 DPI)